Palaeogeography, Palaeoclimatology, Palaeoecology 448 (2016) 26–38

Contents lists available at ScienceDirect

Palaeogeography, Palaeoclimatology, Palaeoecology

journal homepage: www.elsevier.com/locate/palaeo

High-resolution SIMS oxygen isotope analysis on conodont apatite from South China and implications for the end-Permian mass extinction

Jun Chen [a,*], Shu-zhong Shen [b], Xian-hua Li [c], Yi-gang Xu [a], Michael M. Joachimski [d], Samuel A. Bowring [e], Douglas H. Erwin [f], Dong-xun Yuan [b], Bo Chen [b], Hua Zhang [b], Yue Wang [b], Chang-qun Cao [b], Quan-feng Zheng [g], Lin Mu [h]

[a] State Key Laboratory of Isotope Geochemistry, Guangzhou Institute of Geochemistry, Chinese Academy of Sciences, Guangzhou 510640, China
[b] State Key Laboratory of Palaeobiology and Stratigraphy, Nanjing Institute of Geology and Palaeontology, Chinese Academy of Sciences, Nanjing 210008, China
[c] State Key Laboratory of Lithospheric Evolution, Institute of Geology and Geophysics, Chinese Academy of Sciences, Beijing 100029, China
[d] GeoZentrum Nordbayern, Universität Erlangen-Nürnberg, Schlossgarten 5, 91054 Erlangen, Germany
[e] Department of Earth, Atmospheric, and Planetary Sciences, Massachusetts Institute of Technology, 77 Massachusetts Avenue, Cambridge, MA 02139, USA
[f] Department of Paleobiology, National Museum of Natural History, Smithsonian Institution, MRC-121, Washington, DC 20013-7012, USA
[g] Key Laboratory of Economic Stratigraphy and Palaeogeography, Nanjing Institute of Geology and Palaeontology, Chinese Academy of Sciences, Nanjing 210008, China
[h] Department of Invertebrate Palaeontology, Nanjing Institute of Geology and Palaeontology, Chinese Academy of Sciences, Nanjing 210008, China

ARTICLE INFO

Article history:
Received 30 July 2015
Received in revised form 19 November 2015
Accepted 23 November 2015
Available online 3 December 2015

Keywords:
SIMS
Oxygen isotope
Conodont apatite
South China
Climate warming
End-Permian mass extinction

ABSTRACT

Understanding the interplay of climatic and biological events in deep time requires resolving the precise timing and pattern of paleotemperature changes and their temporal relationship with carbon cycle variations and biodiversity fluctuations. In situ oxygen isotope analyses of conodont apatite from South China enables us to reconstruct high-resolution seawater temperature records across the Permian–Triassic boundary (PTB) intervals in the upper slope (Meishan), lower slope (Shangsi), and carbonate platform (Daijiagou and Liangfengya) settings. Constrained by the latest high-precision geochronological dates and high-resolution conodont biozones, we can establish the temporal and spatial patterns of seawater temperature changes and assess their potential connections with the carbon cycle disruption and biodiversity decline. We find a rapid warming of ~10 °C during the latest Permian–earliest Triassic that postdated the onset of the negative shift in $\delta^{13}C_{carb}$ by ~81 kyr (thousand years), the abrupt decline in $\delta^{13}C_{carb}$ by ~32 kyr and the onset of mass extinction by ~23 kyr, which contradicts previous claims that the extreme temperature rise started immediately before or coincided with the onset of mass extinction. Our new evidence indicates that climate warming was most likely not a direct cause for the main pulse of the end-Permian mass extinction (EPME), but rather a later participant or a catalyst that increased the pace of the biodiversity decline. In addition, a prominent cooling is recorded in the earliest Changhsingian, with the main phase (a drop of ~8 °C in ~0.2 Ma) confined to the lower part of the *Clarkina wangi* zone and synchronous with the positive limb of the carbon isotope excursion (CIE) around the Wuchiapingian–Changhsingian boundary (WCB) in Meishan and Shangsi. Further long-term and high-resolution studies from other sections are needed to confirm the full contexts and underlying dynamics of the WCB "cooling event".

1. Introduction

The catastrophic EPME has long been recognized as the most severe crisis during the Phanerozoic, and marked a fundamental shift in Earth's ecological structure (Raup and Sepkoski, 1982). Numerous hypotheses have been proposed as the cause(s) of this cataclysm, including bolide impact, ocean anoxia, and flood basalt volcanism (Knoll et al., 2007; Payne and Clapham, 2012). Severe environmental perturbations related to the Siberian Traps volcanism have been considered by many as one of the most plausible scenarios for the killing mechanism (Campbell et al., 1992; Renne et al., 1995; Kamo et al., 2003; Svensen et al., 2009; Black et al., 2012). This "favored" hypothesis has received strong support from recent high-precision geochronological dates from the Meishan stratotype section (Burgess et al., 2014) and the Siberian Traps (Burgess and Bowring, 2015). A new age model (Burgess and Bowring, 2015) of the Siberian Traps volcanism (explosive, effusive, and intrusive) demonstrated that pyroclastic and lava eruptions predated the onset of the EPME by 300 ± 126 kyr, supporting a causal connection. Furthermore, two-thirds of an estimated 4×10^6 km^3 of magma were emplaced/erupted over this ~300-kyr interval, before and during the mass extinction interval. The bulk of intrusive activity

* Corresponding author at: State Key Laboratory of Isotope Geochemistry, Guangzhou Institute of Geochemistry, Chinese Academy of Sciences, 511 Kehua Street, Wushan, Tianhe District, Guangzhou 510640, China. Tel./fax: +86 20 85290030.
E-mail address: junchen@gig.ac.cn (J. Chen).

http://dx.doi.org/10.1016/j.palaeo.2015.11.025
0031-0182/

began within the mass extinction interval (within 61 ± 48 kyr; Burgess et al., 2014) and continued for at least 500 kyr after the cessation of mass extinction.

Although the temporal overlap between the Siberian Traps volcanism and the EPME links the two events, many questions remain unresolved about the nature of the connection. For example, which pulse of the Siberian Traps volcanism is responsible for the EPME? What is the underlying dynamic behind such disparity between the volcanism and biotic crisis? Resolving such questions requires establishing a precise timeline between the environmental deterioration and biodiversity decline, since most large igneous province eruptions (Wignall, 2001; Bond and Wignall, 2014) are expected to impact the Earth's climate via carbon cycle disruption, short-term cooling followed by long-term warming, and ocean acidification. The negative shift of $\delta^{18}O$ in whole rock carbonates from the Carnic Alps of Austria initially suggested climate warming of ~5–6 °C around the PTB, although the possible influences from salinity and/or diagenesis cannot be excluded (Holser et al., 1989), which makes such whole rock $\delta^{18}O$ record unreliable. Conodont apatite is preferred to whole rock carbonates and brachiopod calcites due to its resistance to diagenesis (Luz et al., 1984; Wenzel et al., 2000). Thus the $\delta^{18}O$ signature of conodonts is widely regarded as an applicable proxy for reconstruction of seawater temperatures in the Paleozoic and Triassic (Trotter et al., 2008, 2015; Joachimski et al., 2012; Sun et al., 2012; Romano et al., 2013). Using this methodology, climate change around the EPME was demonstrated on the basis of $\delta^{18}O$ data derived from conodont apatite in South China and Iran. These results indicated that the major seawater temperature increase started immediately before (Joachimski et al., 2012) or at the mass extinction horizon (Schobben et al., 2014) and suggested climate warming as one of the causes of the EPME.

Owing to the absence of oxygen isotope data from Bed 25 in Meishan, the base of which corresponding to the onset of the EMPE (Jin et al., 2000; Shen et al., 2011; Wang et al., 2014), it was ambiguous whether the increase of temperatures predates, coincides with, or postdates the onset of mass extinction. Also, available $\delta^{18}O$ data across the EPME (Joachimski et al., 2012; Schobben et al., 2014) were all derived from the conventional isotope ratio mass spectrometry (IRMS) method, which requires large sample size (>0.5 mg, or 10–50 specimens depending on the size/weight of individuals) and analyzes on "bulk" materials. Since conodonts near the PTB are mostly small in size and of low abundance, particularly within the EPME interval and above, low-yielding conodont samples were excluded from the IRMS analyses, thus reducing the much needed temporal resolution.

Understanding the interplay between climatic and biological events around the EPME requires resolving the precise timing and pattern of paleotemperature changes and their temporal relationship with carbon cycle variations and biodiversity fluctuations, which is the aim of this contribution, undertaken through the combination of analytical method, materials selection, and updated temporal framework:

(1) In situ SIMS method. We overcome the limitation of conventional IRMS analyses (i.e., sample size) by measuring oxygen isotope compositions of individual conodont elements using the in situ secondary ion mass spectrometry (SIMS) method. To eliminate as many diagenetic and preservation artifacts as possibly we followed strict analytical procedures (see Supplementary material for details) and applied with considerable caution on the $\delta^{18}O$ variability (Wheeley et al., 2012; Zigaite and Whitehouse, 2014). This technique has been proven to have considerable potential for reconstructing paleoclimate and paleoceanography (Trotter et al., 2008, 2015; Rigo et al., 2012; Wheeley et al., 2012), and can significantly increase the spatial and temporal resolutions based on samples with low-yielding conodont elements.

(2) Multiple stratigraphic sections. To resolve the temporal and spatial pattern of paleotemperature changes across the EPME interval, we generated high-resolution in situ oxygen isotope data from four sections in South China (Meishan, Shangsi, Daijiagou and Liangfengya). We selected the condensed Meishan and Shangsi sections, since extensive studies from both sections have produced integrated, high-resolution geochronological dates (Shen et al., 2011; Burgess et al., 2014), carbon isotopes (Shen et al., 2013), and conodont biostratigraphy (Shen et al., 2013; Yuan et al., 2014). Published IRMS data from both sections (Joachimski et al., 2012; Chen et al., 2013) were also available for comparison with our new SIMS records. Samples from the well-studied Daijiagou (Yuan et al., 2015) and Liangfengya (Yuan and Shen, 2011) sections were also analyzed; both sections were deposited on a shallow carbonate platform during the Permian–Triassic transition, in contrast to Meishan (upper slope) and Shangsi (lower slope) and thus can be used for spatial comparison.

(3) Uniform temporal framework. To constrain the timing and rate of paleotemperature changes, the stratigraphic depth of all samples are adjusted to a uniform timescale, mainly based on the latest U–Pb ages (Shen et al., 2011; Burgess et al., 2014) and conodont zones (Yuan et al., 2014) from Meishan to correlate with other sections. This results in a high-resolution, time dependent record for the latest Permian–earliest Triassic interval.

2. Studied sections and materials

Conodont samples used in this study were collected from four sections in South China (Fig. 1), which were located at a paleolatitude of ~25 N° on the Yangtze carbonate platform and its northern marginal basin in the eastern Palaeotethys Ocean during the Late Permian–Early Triassic (Stampfli and Borel, 2004). Sequence stratigraphy and facies analysis (Shen and He, 1991; Shen and Shi, 1995; Wignall and Hallam, 1996; Yin et al., 2001; Song et al., 2013) indicated that the studied sections were deposited in different environmental settings around the PTB, including the upper slope (Meishan), lower slope (Shangsi), and carbonate platform (Daijiagou and Liangfengya). Details on studied sections (Fig. 2) and materials can be found in the Supplementary material.

3. Biostratigraphic correlation and temporal framework

High-resolution Late Permian–Early Triassic conodont biostratigraphy (Shen and Mei, 2010; Shen et al., 2010), lithostratigraphy (Cao and Zheng, 2007; Yin et al., 2014), and $\delta^{13}C_{carb}$ chemostratigraphy (Shen et al., 2013) allowed us to correlate the sections with the newly revised conodont-based integrated records from the Meishan stratotype section (Yuan et al., 2014) serving as the standard. After thorough evaluation, the published conodont zones from Shangsi (Jiang et al., 2011; Shen et al., 2011, 2013), Daijiagou (Yuan et al., 2015), and Liangfengya (Yuan and Shen, 2011) were directly applied or accordingly modified as biostratigraphic constraints for intra-regional correlations (Supplementary Tables S1–4).

Several baselines for correlation were first established: (1) The PTB is at 42.11 m in Meishan, 100.4 m in Shangsi, 0.58 m in Daijiagou, and 0 m in Liangfengya, defined by the first appearances of *Hindeodus parvus*, except for Shangsi where the first occurrence of *H. parvus* was proven to be younger than many other occurrences including the FAD (First Appearance Datum) (Nicoll et al., 2002; Henderson, 2006; Jiang et al., 2011). *Hindeodus eurypyge* was regarded as an alternative index for our definition of the PTB in Shangsi (Shen et al., 2011, 2013), that is at the same level as in the restudy of Jiang et al. (2011) where the first occurrences of *Clarkina taylorae* and *Hindeodus changxingensis* defined the PTB. (2) The onset of the EPME is defined at the base of Bed 25 (41.93 m) at Meishan (Jin et al., 2000; Shen et al., 2011; Wang et al., 2014), corresponding to the base of Bed 27 (100.1 m) at Shangsi (Shen et al., 2011, 2013), the base of "boundary clay" (0 m) at Daijiagou (Shen and Shi, 1995), and the base of Bed 29 (−0.51 m) at Liangfengya

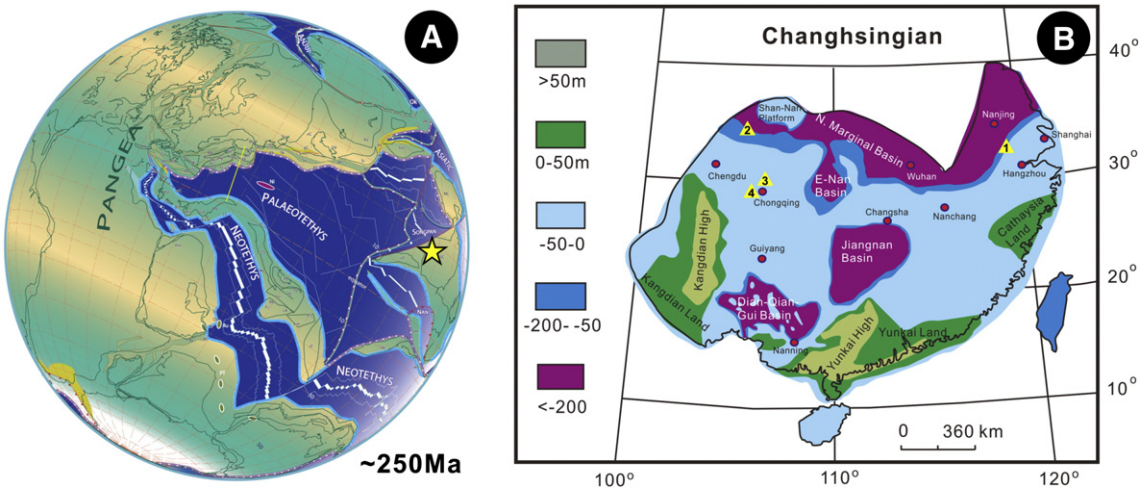

Fig. 1. (A) Paleogeographic reconstruction for the Late Permian (Stampfli and Borel, 2004) and (B) locality map (Shen et al., 2013) showing the positions of studied sections in South China. 1. Meishan; 2. Shangsi; 3. Daijiagou; 4. Liangfengya.

(Yuan and Shen, 2011). (3) The WCB is at 0.88 m (base of Bed 4a-2) in the Meishan stratotype section (Jin et al., 2006) and 84.0 m in Shangsi (Shen et al., 2011, 2013), both of which were defined by the first appearances of *Clarkina wangi*. The exact position of the WCB in Daijiagou is unclear since only sparse conodonts have been recovered from this interval (Yuan et al., 2015). The WCB in Liangfengya is also difficult to determine, although early study at the nearby Beifengjing section (Shen and Shi, 2002) suggested that the base of the Changhsingian is likely ca. 91.5 m below the PTB.

In addition to the conodont zones assigned to each sample, numeric age estimates were also allocated on the basis of sediment accumulation rate calculations for specific intervals in each section (see details in Supplementary Tables S1–4). In the extensively studied Meishan section, the WCB, the onset of the EPME, and the PTB were constrained by recent high-precision geochronology as 254.14 ± 0.07 Ma (Shen et al., 2011), 251.941 ± 0.037 Ma (Burgess et al., 2014), and 251.902 ± 0.024 Ma (Burgess et al., 2014), respectively. Along with ages from other dated ash beds (Shen et al., 2011; Burgess et al., 2014), a high-resolution temporal framework can be established for the WCB-PTB interval in Meishan.

Twelve ash beds from Shangsi have been dated previously; eight of them produced reliable ages which were in agreement with results from the Meishan section at the time they were published (Shen et al., 2011). Subsequent improvements in U–Pb geochronology yielded more precise and accurate ages in Meishan (Burgess et al., 2014), but such updates are currently unavailable for the Shangsi section. For the convenience of high-precision correlation in a uniform temporal framework, we only use updated ages from Meishan (PTB, mass extinction,

Fig. 2. Field photos showing the PTB intervals at Meishan (A), Shangsi (B), Daijiagou (C), and Liangfengya (D), with the onset of the end-Permian mass extinction and the P–T boundary marked as red and green lines, respectively.

and WCB) to calibrate our samples from Shangsi, Daijiagou, and Liangfengya (Supplementary Tables S1–4).

4. In situ SIMS method

Using in situ SIMS technique to measure the oxygen isotope composition of conodont apatite (Trotter et al., 2008, 2015; Rigo et al., 2012; Wheeley et al., 2012), foraminiferal calcite (Kozdon et al., 2009, 2011), and other faunal materials (Aubert et al., 2012; Blumenthal et al., 2014; Zigaite and Whitehouse, 2014) have been well developed in recent years, with similar analytical procedures among different laboratories. At the CA-SIMS laboratory in the Institute of Geology and Geophysics, Chinese Academy of Sciences, we used a Cameca IMS-1280 SIMS, generally following the methodology developed in the SHRIMP laboratory of the Australian National University (Trotter et al., 2008, 2015). Detailed analytical procedures and protocols are presented in the Supplementary material.

5. Results

Rather than focusing on the mass extinction interval alone, our in situ $\delta^{18}O_{apatite}$ records extend to the latest Wuchiapingian (top of the *Clarkina longicuspidata* zone) in Meishan (Figs. 3, 4) and the earliest Changhsingian (base of the *C. wangi* zone) in Shangsi (Fig. 5), thus placing the PTB events within a long-term context. $\delta^{18}O_{apatite}$ data across the WCB in Meishan (Fig. 3) show a prominent increase (~2‰), which began immediately above the WCB (MSD 4a-3, 1.07 m, 19.2‰), and extended into the lower part of the *C. wangi* zone (MSD 4b-11, 2.59 m, 21.0‰). Although not as in high-resolution as in Meishan, data from the earliest Changhsingian in Shangsi suggest a similar pattern, which started at 20.3‰ (SHS-283.4, 84.57 m, base of the *C. wangi* zone) and

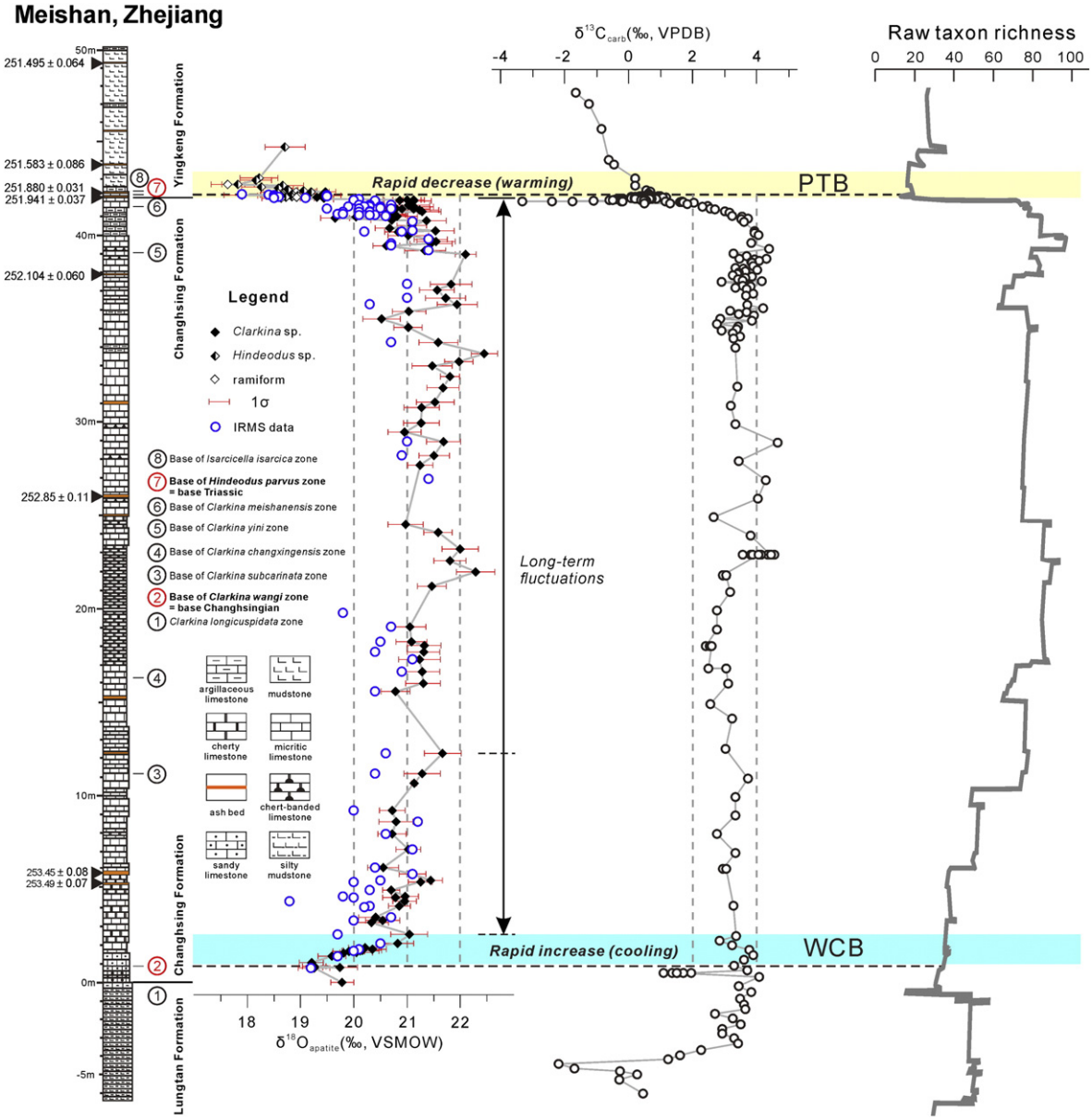

Fig. 3. Compiled $\delta^{18}O_{apatite}$ record (including new in situ SIMS data in this study, and published IRMS data from Joachimski et al., 2012; Chen et al., 2013), $\delta^{13}C_{carbon}$ record (Shen et al., 2013; Burgess et al., 2014), and raw taxon richness curve (generated by Y. Wang using CONOP) from the Meishan stratotype section, all scaled to the thickness of strata. Lithology, revised conodont biozones (see details in Supplementary Tables S1) (Yuan et al., 2014), and U–Pb ages for dated ash beds (Shen et al., 2011; Burgess et al., 2014) are provided. Cyan band represents the prominent increase of $\delta^{18}O_{apatite}$ (cooling) in the lower part of the *C. wangi* zone; light yellow band indicates the rapid decrease of $\delta^{18}O_{apatite}$ (warming) above the mass extinction horizon; and the span in between is regarded as the long-term fluctuations interval.

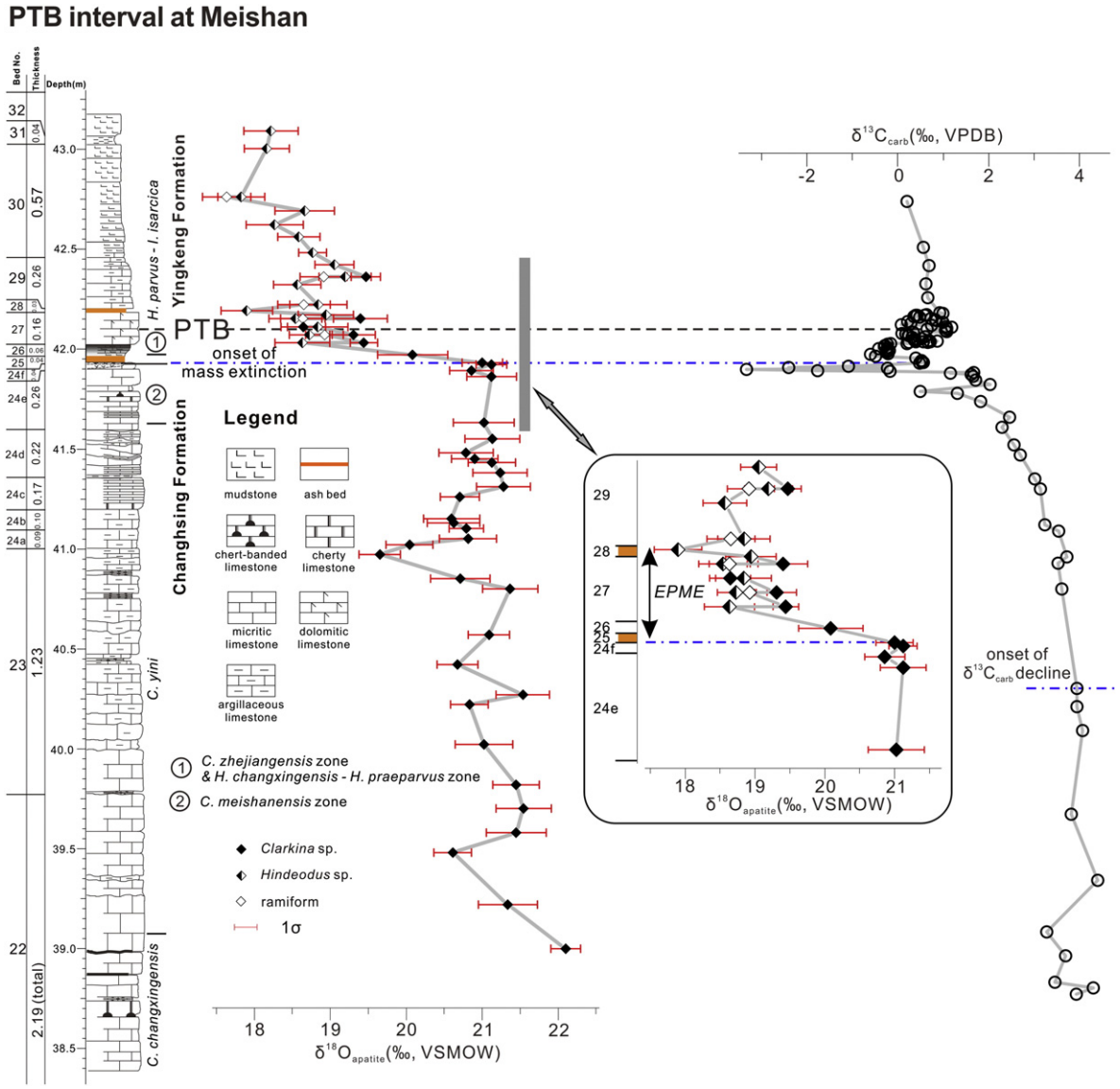

Fig. 4. Close-up of in situ $\delta^{18}O_{apatite}$ and $\delta^{13}C_{carbon}$ records across the latest Permian–earliest Triassic interval at Meishan, with insert of high-resolution in situ $\delta^{18}O_{apatite}$ data prior to, during, and after the EPME. Lithology, number and thickness of each bed, and conodont zones are presented. Note that immediately before the EPME (i.e., Bed 24e–f) and at the mass extinction horizon (i.e., Bed 25), $\delta^{18}O_{apatite}$ values remain high as ~21‰, which clearly indicates no elevation in seawater temperatures at the onset of the EPME.

ended at 20.6‰ (SHS-285.0, 86.13 m, lower part of the *C. wangi* zone) (Fig. 5). Without sufficient data below the WCB in both Meishan and Shangsi to constrain the "real" initiation of this positive shift in $\delta^{18}O_{apatite}$, we tentatively suggest that the increasing phase is confined in the *C. wangi* zone.

Above the increasing phase in the *C. wangi* zone and below the base of the *Clarkina yini* zone, $\delta^{18}O_{apatite}$ values from both Meishan and Shangsi (Figs. 3, 5) are comparable and fluctuate around ~21‰. Detailed evaluation of $\delta^{18}O_{apatite}$ data from this interval in Meishan shows several shifts, such as the decrease from 22.5‰ (MSD 19-17, 33.69 m) to 20.5‰ (MSD 20-2a–2b, 35.55 m), followed by an immediate return to 22.1‰ (MSD 22-10-base, 39.00 m), both of which occurred at the top of the *Clarkina changxingensis* zone. Due to different sampling intensities, such shifts in the better resolved Meishan section cannot be confirmed in Shangsi, Daijiagou, and Liangfengya (Figs. 5–7).

High-resolution data above the base of the *C. yini* zone from all four studied sections (Figs. 4–7) enabled us to correlate and compare the pattern and magnitude of $\delta^{18}O_{apatite}$ changes in different environmental settings. (1) The general trends are nearly identical among four sections: prior to the onset of the EPME, $\delta^{18}O_{apatite}$ values are high (20.5–21.5‰ in Meishan, 20.0–21.0‰ in Shangsi, 19.0–20.0‰ in Daijiagou, and 18.5–19.5‰ in Liangfengya); a dramatic negative shift occurred above the extinction horizon, with comparable magnitude of 2.5–3.0‰ across the four sections. Close observations indicate that a mild decrease occurs in the *C. yini* zone and is followed by a return to the pre-shift level at the mass extinction horizon. As for the minimum of $\delta^{18}O_{apatite}$ value, it appears in the middle-to-top of the *C. yini* zone at Meishan and Shangsi but near the very top at Daijiagou and Liangfengya. (2) Data across the mass extinction horizon from all sections suggests that the prominent decrease of $\delta^{18}O_{apatite}$ values occurred after the onset of the EPME. Using high-resolution data from the well-constrained Meishan section as an example (Fig. 4), $\delta^{18}O_{apatite}$ values remain as high as 21.0‰ throughout Beds 24e to 25 (on *Clarkina*), decrease to 20.1‰ in Bed 26 (on *Clarkina*), dramatically drop to 19.4‰ (on *Clarkina*) or 18.6‰ (on *Hindeodus*) in Bed 27-1, and reach the first low of 17.9‰ in Bed 28 (on *Hindeodus*) and the second low of 17.6‰ in Bed 30-5 (on ramiforms). Given the potential offset between *Clarkina* and *Hindeodus* (Joachimski et al., 2012; Chen et al., 2013), a conservative comparison based on *Clarkina* alone indicates that the decrease to 19.4‰ occurred in Bed 27-1, thus the rapid drop in $\delta^{18}O_{apatite}$ postdated

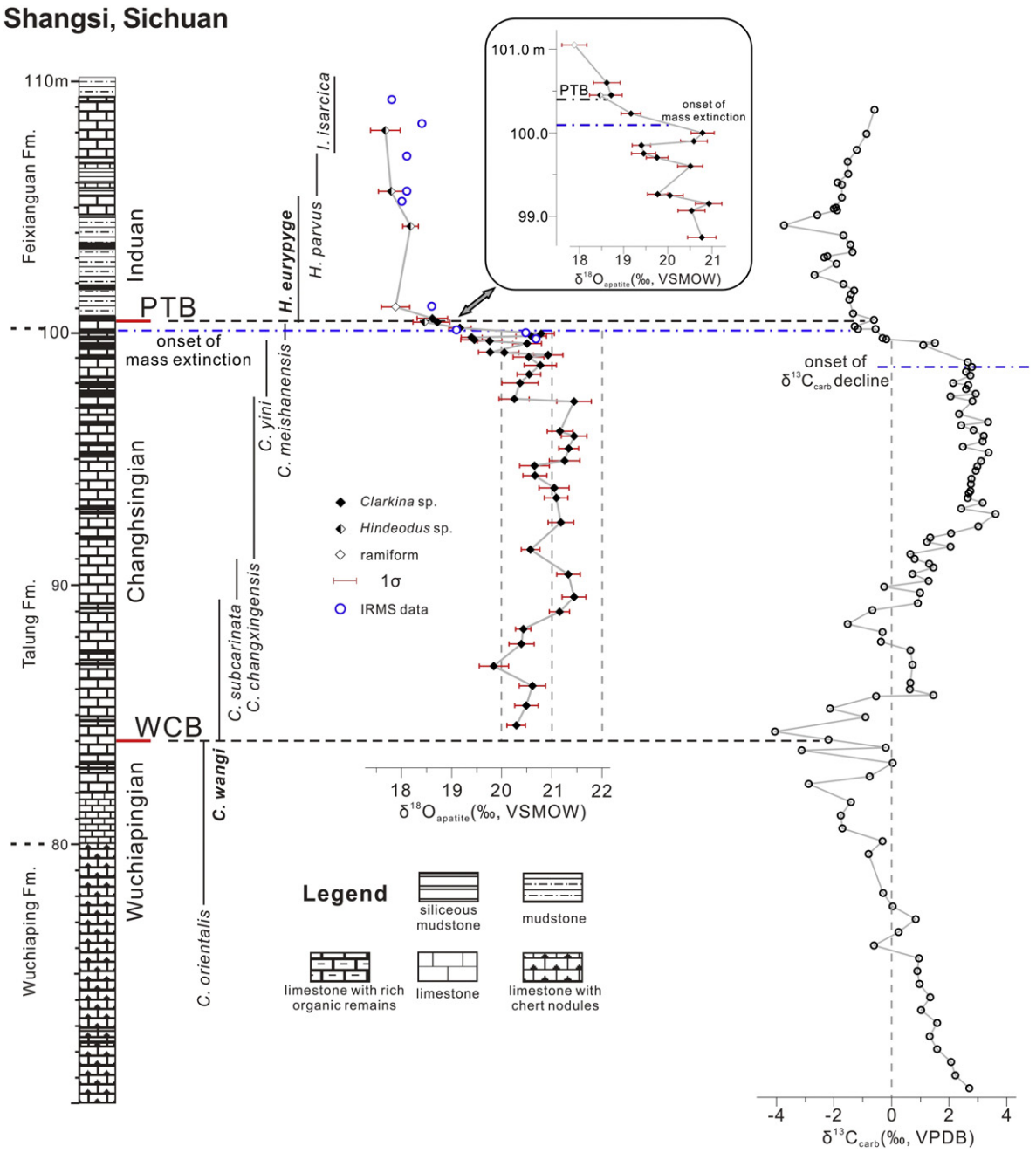

Fig. 5. $\delta^{18}O_{apatite}$ (including new in situ SIMS data in this study, and published IRMS data from Joachimski et al., 2012) and $\delta^{13}C_{carbon}$ records from the Shangsi section, all scaled to the thickness of strata. Lithology, conodont zones (see details in Supplementary Tables S2), and insert of high-resolution in situ $\delta^{18}O_{apatite}$ data across the EPME are provided.

the onset of the EPME. (3) Although the magnitude of significant decrease above the EPME horizon is generally consistent among four sections (2.5–3.0‰), the distinct difference lies with the absolute $\delta^{18}O_{apatite}$ values. For instance, $\delta^{18}O_{apatite}$ values at the mass extinction horizon are ca. 21.0‰ in Meishan and Shangsi, which is about 1.0–1.5‰ higher than those in Daijiagou and Liangfengya. Whether such offsets are related to the differences in environmental setting or CAI value of conodont elements (see Supplementary material for details) is unclear, and requires further study based on more systematic datasets. Nonetheless, our conclusions are not affected by such offsets, since the primary concern is about the temporal relationship between the sudden decrease in $\delta^{18}O_{apatite}$ and the onset of the EPME, and also whether such pattern can be confirmed across studied sections.

High-precision temporal framework enabled us to assess the timing and rate of $\delta^{18}O_{apatite}$ changes during the Late Permian–earliest Triassic, especially around the EMPE interval (Fig. 8) when the timeline of the well constrained end-Permian carbon isotope excursion (CIE) and mass extinction can be associated. If one accepts that the main phase of positive shift of $\delta^{18}O_{apatite}$ around the WCB is only confined to the lower part of the *C. wangi* zone (Fig. 3), calculation based on our age estimates suggests a prominent rise of ~2‰ occurred in about 0.2 Ma (Fig. 8A). After this rapid increase around the WCB and prior to the dramatic decrease that postdated the onset of the EPME, the long-term fluctuations during most of the Changhsingian are around a baseline of ~21‰. About 0.1 Ma before the onset of the EPME, comparable data indicate no substantial shifts in $\delta^{18}O_{apatite}$ (Fig. 8B). Timing of the transient change (mild decrease followed by a return) prior to the onset of the EPME is inconsistent among studied sections, which appeared slightly earlier in Meishan and Shangsi but more close to the onset of the EPME in Daijiagou and Liangfengya, thus indicating local controls

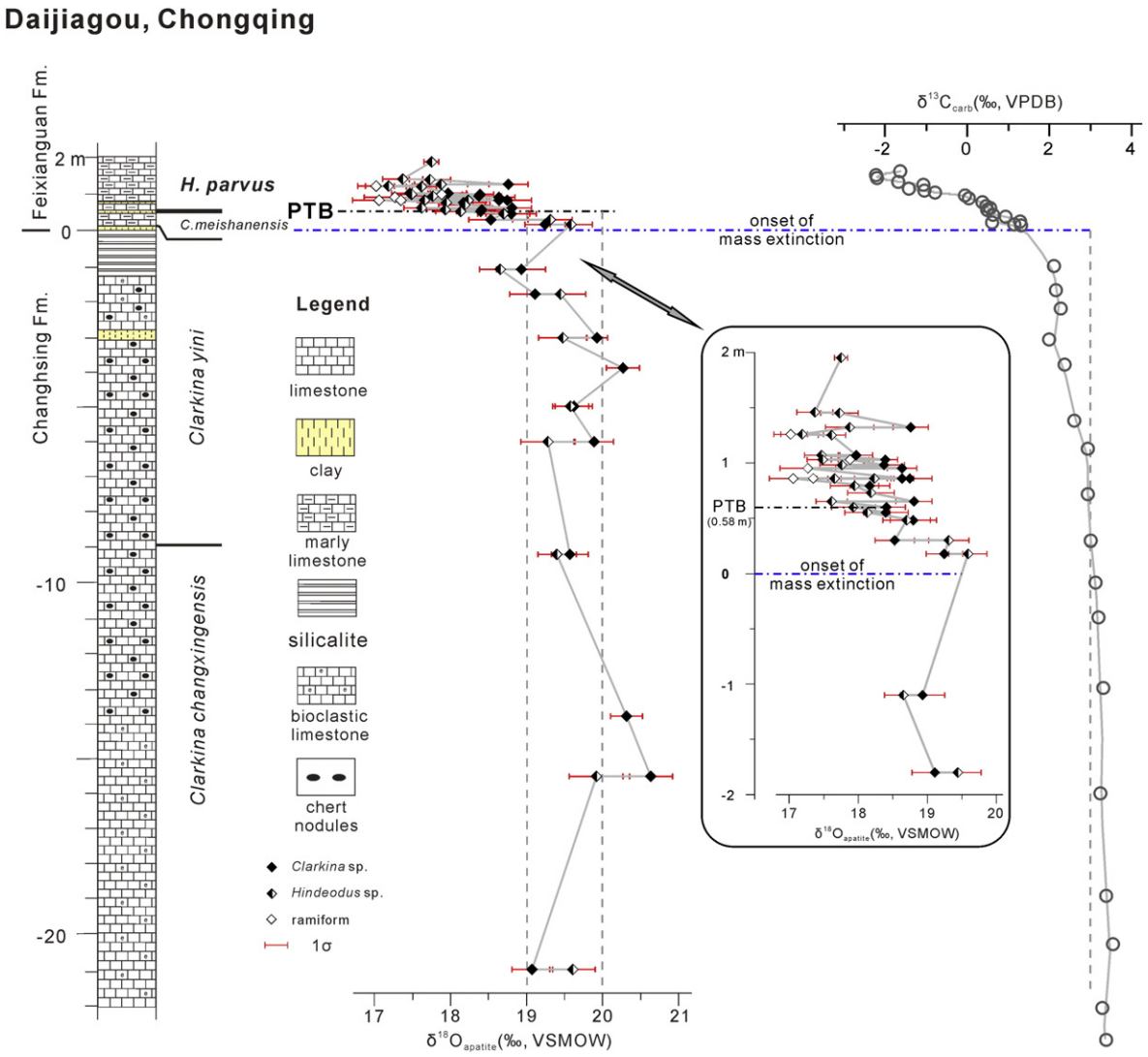

Fig. 6. $\delta^{18}O_{apatite}$ and $\delta^{13}C_{carbon}$ records from the Daijiagou section, all scaled to the thickness of strata. Insert showing the close-up of the $\delta^{18}O_{apatite}$ data from the EPME interval; ranges of conodont species, $\delta^{13}C_{carbon}$ and its correlation with other PTB sections can be found in Yuan et al., 2015.

rather than global climatic events. Latest geochronological dates from Meishan (Burgess et al., 2014) constrained the onset of the CIE, the abrupt decline in $\delta^{13}C_{carb}$, the onset of the EMPE, the PTB, and the cessation of the EPME at 251.999 Ma, 251.950 Ma, 251.941 Ma, 251.902 Ma, and 251.880 Ma, respectively. If one accepts the substantial decrease of $\delta^{18}O_{apatite}$ at 251.918 Ma (corresponding to the base of Bed 27-1 in Meishan; Figs. 4, 8B), a straightforward calculation suggests that the significant warming occurred ~81 kyr after the onset of the CIE, ~32 kyr after the abrupt decline in $\delta^{13}C_{carb}$, and ~23 kyr after the onset of the EPME.

6. Discussions

6.1. SIMS and IRMS comparison

The techniques for analyzing oxygen isotope compositions of biogenic phosphates as paleoenvironmental proxies have been well developed (Kolodny et al., 1983; Shemesh et al., 1983; Luz et al., 1984; Luz and Kolodny, 1985). As biogenic apatite, conodonts can be described by the general formula $Ca_5Na_{0.14}(PO_4)_{3.01}(CO_3)_{0.16}F_{0.73}(H_2O)_{0.85}$ (Pietzner et al., 1968), with oxygen presented in three different sites of the mineral. The conventional IRMS method isolates the PO_4^{3-} group as Ag_3PO_4, which is then converted to CO as the analyte gas for oxygen isotope measurements (O'Neil et al., 1994; Joachimski et al., 2009). By comparison, the in situ SIMS technique utilizes Cs^+ primary ion beam to bombard the exposed smooth surfaces of untreated biogenic phosphates and releases oxygen from all O-bearing compounds (PO_4^{3-}, CO_3^{2-}, and OH^-). Given the difference in analytical principles, offsets between paired $\delta^{18}O_{apatite}$ values derived from IRMS and SIMS methods are expected. Calculations by Wheeley et al. (2012) suggested that the shift in values from a purely PO_4^{3-} signal is likely to be of the order of +0.02–0.7‰ and was supported by paired data from two Silurian conodont samples measured by both SIMS and IRMS techniques, which show offsets of ca. 0.5‰ and 1.0‰ for *Ozarkodina* and *Panderodus*, respectively. Measurements on modern shark teeth enameloid suggested that the SHRIMP $\delta^{18}O_{apatite}$ values are systematically higher than IRMS values, such as 0.7‰ (Trotter et al., 2008) or typically by ~0.6–1.3‰ (Trotter et al., 2015).

Among the 128 samples from Meishan measured with the in situ SIMS technique, 63 have been analyzed with the conventional IRMS method (Joachimski et al., 2012; Chen et al., 2013), which provides us an opportunity to constrain the offset with larger datasets. The

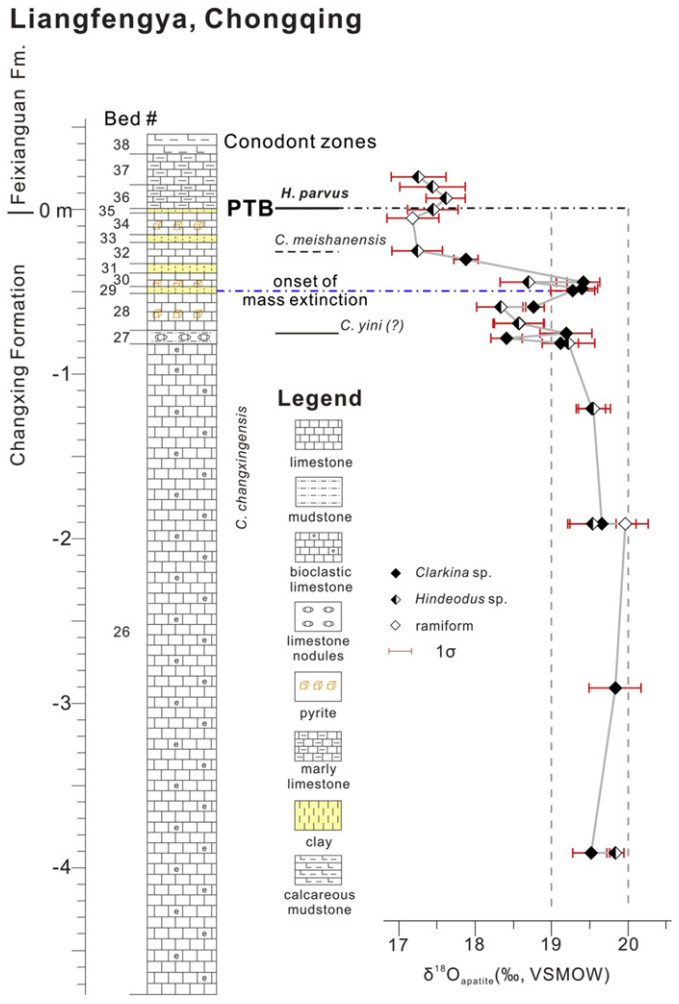

Fig. 7. $\delta^{18}O_{apatite}$ record from the Liangfengya section, scaled to the thickness of strata. Bed numbers and lithology from Shen and He (1991), but see a more recent description in Yuan and Shen (2011) where conodont biostratigraphy was also presented.

phosphorite standard NBS 120c is widely used in the IRMS analyses, and both 21.7‰ and 22.6‰ have been reported (Joachimski et al., 2012; Sun et al., 2012; Chen et al., 2013; Schobben et al., 2014). Although the NBS 120c standard is distributed in the form of calcium phosphate powder that cannot be directly measured with the in situ SIMS method, it was used in the IRMS analyses to determine the $\delta^{18}O_{apatite}$ values of our Durango standard (Supplementary Table S6). To compare the IRMS and SIMS data from Meishan, the earlier published IRMS $\delta^{18}O_{apatite}$ values (Joachimski et al., 2012; Chen et al., 2013) were adjusted by subtracting 0.9‰ (Supplementary Database S2, Table S7) based on the now accepted value of NBS 120c of 21.7‰ (Lécuyer et al., 2013). After adjustment, a comparison between the corrected IRMS values and our in situ SIMS data (Fig. 9A) shows that the two datasets are linearly correlated and can be expressed by the following regression:

$$\delta^{18}O_{SIMS} = (0.96 \pm 0.08)\delta^{18}O_{IRMS} + (1.31 \pm 1.70),\ R^2 = 0.68.$$

Pearson correlation coefficient also suggests a positive relationship (Pearson's $r = 0.82$, $p = 0.00$, n = 63). The SIMS values are generally higher than the IRMS ones, with an average offset of +0.5‰ ($\Delta = \delta^{18}O_{SIMS} - \delta^{18}O_{IRMS}$, Max. = +2.2, Min. = −0.9); if excluding the rare abnormal data, the offset is typically ~0.0–1.0‰ (average of +0.5‰; Fig. 9B), which is consistent with the reported biases (Trotter et al., 2008, 2015; Wheeley et al., 2012). There is no correlation between the offsets and the stratigraphic depths, thus indicating the offsets are consistently within a specific range (0 to 1‰) that is not time dependent.

6.2. Paleotemperature calculations

Since the establishment of the phosphate $\delta^{18}O$ thermometer (Kolodny et al., 1983), several revisions of the phosphate–water fractionation and temperature calibration have been published and no consensus has been reached (Pucéat et al., 2010; Lécuyer et al., 2013; Chang and Blake, 2015). Calculation of seawater temperatures in deep time is subject to some uncertainties. On the premise that $\delta^{18}O$ values measured on conodont apatite are precise and accurate, oxygen isotope composition of seawater from which they precipitate is another variable that determining the calculated temperatures. Although we cannot directly measure $\delta^{18}O_{seawater}$, it has been suggested that the secular variations in global mean $\delta^{18}O_{seawater}$ are generally around 0 ± 1‰ (VSMOW) (Jaffrés et al., 2007), following the glacial–interglacial cycles due to the significant effect from ^{18}O depleted glacial meltwater (Lhomme et al., 2005). For the "ice-free" Late Permian–Early Triassic world (Chumakov and Zharkov, 2003), $\delta^{18}O_{seawater}$ of −1‰ (VSMOW) is commonly adopted in paleotemperature calculations (Joachimski et al., 2012; Rigo et al., 2012; Sun et al., 2012; Romano et al., 2013; Trotter et al., 2015).

Salinity and ice volume are the two main unknowns affecting $\delta^{18}O_{seawater}$, the first of which is dependent on the balance between evaporation and precipitation, and the second is determined by the formation and melting of glacial ice sheets. According to the recently published data from the tropical Pacific Ocean (Conroy et al., 2014), the slope of the regression between $\delta^{18}O_{seawater}$ and salinity is about 0.31‰ psu^{-} in the mixed layer (0–75 m) and 0.42‰ psu^{-} in the subsurface (80–500 m); the salinity–depth relationship suggests that local salinity is generally stable in the mixed layer and subsurface. By this standard, a substantial decrease of 0.5‰ in salinity reflects a decrease of only 0.15‰ in $\delta^{18}O_{seawater}$ for the tropical surface oceans, which is small compared with the uncertainties of $\delta^{18}O_{apatite}$ analyses using IRMS or SIMS. Based on this salinity–depth relationship, in a paleoenvironment such as the Yangtze carbonate platform and its northern marginal basin (Yin et al., 2014), dramatic sea-level changes that would have caused major shift in salinity (Adkins et al., 2002) sufficient to alter the local $\delta^{18}O_{seawater}$ seem unlikely. Consequently, we presume that the influence of salinity on $\delta^{18}O_{seawater}$ was probably minimal. Sedimentological data from eastern Australia (Fielding et al., 2008) indicated eight discrete glacial intervals (C1–C4, and P1–P4) for the Late Paleozoic Ice Age. The timing and duration of the youngest P4 glacial was initially interpreted as 267–260 Ma (Fielding et al., 2008), but recently revised to 260–254.5 Ma based on high-precision dating of tuffs from the Sydney and Bowen basins (Metcalfe et al., 2015). Since our investigated time interval postdates the P4 glacial (Fig. 8A), the potential influence of ice volume can also be disregarded.

By assuming $\delta^{18}O_{seawater}$ is constant at −1‰ (VSMOW), comparisons between calculated temperatures using three different equations (Kolodny et al., 1983; Pucéat et al., 2010; Lécuyer et al., 2013) suggest offsets up to 4 °C (Supplementary Database S2). But since the $\delta^{18}O_{seawater}$ value and the equation used for calculation do not affect the relative changes in temperature, we emphasize the trend and magnitude (Figs. 3–7) rather than the absolute temperatures. Using the recent equation from Lécuyer et al. (2013), a 1‰ shift in $\delta^{18}O_{apatite}$ would correspond to a temperature change of ~4.5 °C, which is the general scale applied to our assessments regarding the magnitude of temperature change.

We also note that the available phosphate $\delta^{18}O$ thermometers (Kolodny et al., 1983; Pucéat et al., 2010; Lécuyer et al., 2013) are only applicable to the IRMS method. If the bias of +0.5‰ between the SIMS and IRMS values is considered valid, in situ $\delta^{18}O_{apatite}$ values

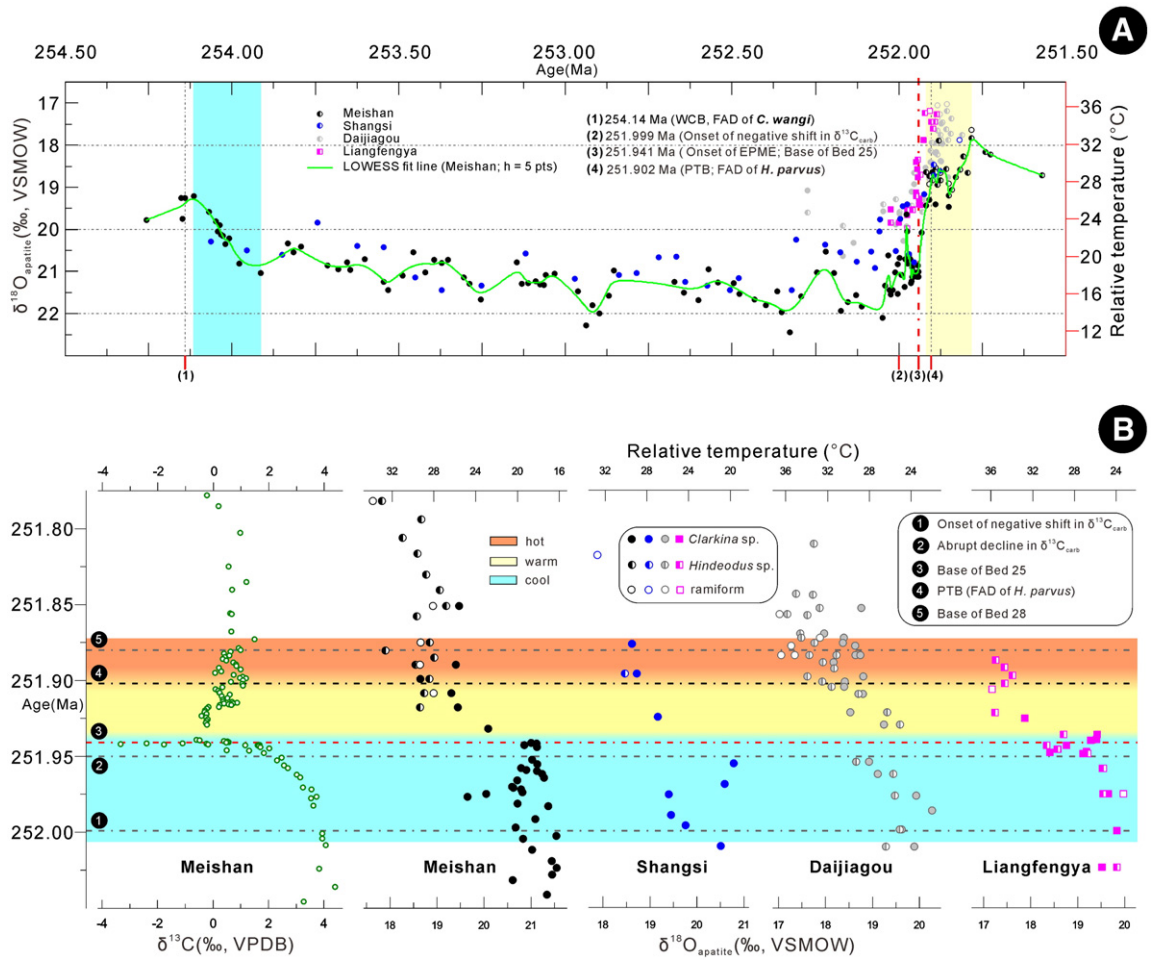

Fig. 8. (A) In situ $\delta^{18}O_{apatite}$ records from Meishan, Shangsi, Daijiagou, and Liangfengya, constrained by a uniform temporal framework to demonstrate the timing and magnitude of changes. Paleotemperature scales are based on the IRMS-based equation from Lécuyer et al. (2013), without considering the average offset of +0.5‰ (this study) between the SIMS and IRMS values. Cyan and light yellow bands represent the prominent "WCB cooling" and "PTB warming" events, respectively. (B) Comparative in situ $\delta^{18}O_{apatite}$ records from the upper slope (Meishan), lower slope (Shangsi), and carbonate platform (Daijiagou and Liangfengya) prior to, during, and after the EPME suggesting a concurrent increase of seawater temperatures (~10 °C) postdates both the abrupt decline in $\delta^{13}C_{carb}$ and the onset of mass extinction, thus indicating climate warming was not a direct cause for the main pulse of the EPME (corresponding to Bed 25 at Meishan). Distinctions for "cool", "warm", and "hot" conditions are relative, not definitive. Paleotemperature scales are also based on the IRMS-based equation from Lécuyer et al. (2013).

need to be systematically reduced by 0.5‰ prior to the temperature calculations using the IRMS-based $\delta^{18}O$ thermometers, and the temperature scales presented in Fig. 8 would shift upwards by ~2.3 °C.

6.3. Climate cooling around the WCB

Our in situ SIMS records from Meishan and Shangsi indicate a prominent cooling around the WCB. Based on current $\delta^{18}O_{apatite}$ datasets (Figs. 3, 5) and paleotemperature calculations, we tentatively suggest that this cooling occurred immediately above the WCB, with the main phase (a drop of ~8 °C in ~0.2 Ma) confined to the lower part of the *C. wangi* zone.

Indications of a Wuchiapingian warming followed by a Changhsingian cooling have been inferred from the fossil evidence in the peri-Gondwanan region (southern Tibet, Salt Range in Pakistan, and Kashmir) (Mei and Henderson, 2001; Shen et al., 2006), which were located in a mesothermal paleolatitude zone and therefore more sensitive to climate change. For instance, the lower part of the Lopingian sequence (upper part of the Wargal Formation and lower part of the Chhidru Formation) in the Salt Range, Pakistan contains numerous compound rugose corals, warm-water brachiopods and conodonts (e.g., *C. longicuspidata*, *C. guangyuanensis*) that are very common in South China, and indicates a warm climate during the Wuchiapingian (Kummel and Teichert, 1970; Shen et al., 2006; Chen et al., 2011, 2013). By contrast, the middle and upper parts of the Chhidru Formation is characterized by typical cold-water brachiopods and conodonts such as *Vjalovognathus* and *Merrillina* (Wardlaw and Mei, 1999; Mei and Henderson, 2001). Along the northwestern margin of Pangaea, the biogenic chert succession in the Sverdrup Basin recorded a significant cooling, which is indicated by siliceous sponge-dominated biota in shallow-water chert (Beauchamp and Baud, 2002). In the southern hemisphere, distal glaciomarine facies of the Wuchiapingian were widely deposited in the Sydney, Bowen, and Tasmania basins (Frank et al., 2015). A similar cooling event around the WCB was also recently reported from the continental Karoo Basin, South Africa (Rey et al., in press). These reports suggest cooler condition in the high-latitude, peri-Gondwanan region during the Wuchiapingian–Changhsingian transition, which is in accord with our seawater temperature records from low-latitude South China.

Previous investigations of the Late Permian–Early Triassic interval have mainly concentrated on the PTB and GLB (Guadalupian–Lopingian boundary) events, thus little was known about climate change in association with perturbations of carbon cycle and biodiversity across the WCB. Our records (Figs. 3, 5) provide temporal constraints on the

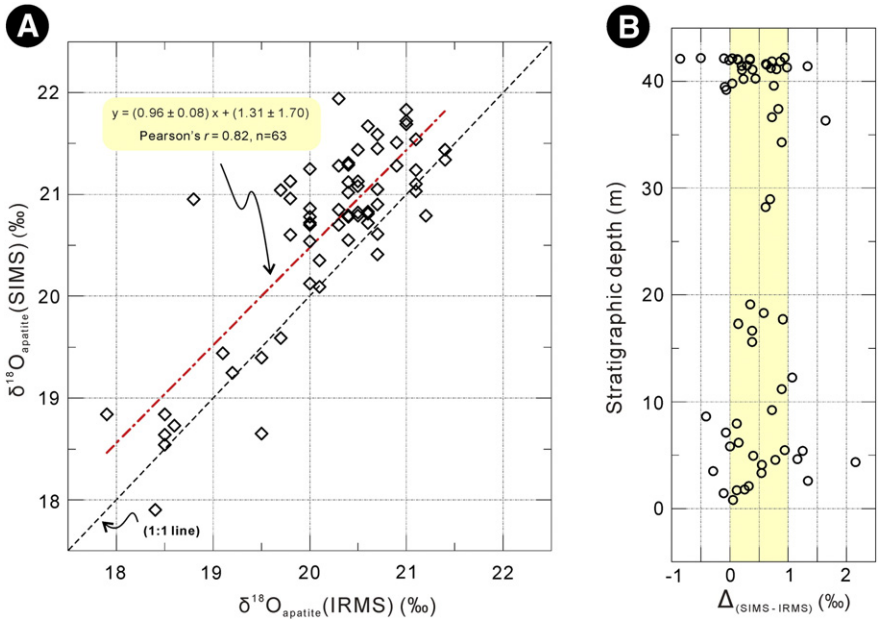

Fig. 9. (A) Comparison between the SIMS and IRMS data based on a suite of 63 samples from Meishan that have been measured by both methods (Supplementary Tables S7), indicating a positive correlation. (B) The differences between paired SIMS and IRMS $\delta^{18}O_{apatite}$ values ($\Delta = \delta^{18}O_{SIMS} - \delta^{18}O_{IRMS}$, Mean = +0.5‰, Max. = +2.2‰, Min. = −0.9‰) against the stratigraphic depth, suggesting the offsets are consistently within a specific range (0 to 1‰) that is not time dependent.

carbon cycle variation, seawater temperature change, and biodiversity pattern during the late Wuchiapingian–early Changhsingian, although the underlying dynamics connecting these changes remain unresolved. Unlike the globally recognized end-Permian CIE, $\delta^{13}C_{carb}$ records around the late Wuchiapingian–early Changhsingian suggested spatial and temporal heterogeneity (Shen et al., 2013). Studied sections in South China demonstrated a broad negative excursion with different magnitudes, such as 6.3‰ in Shangsi, 5.3‰ in Matan, and 2.8‰ in Dukou (Shen et al., 2013). This excursion is truncated in the basal part of the Meishan section (Fig. 3) due to a major regression (Wang et al., 2006), but more completely expressed in the long-ranging Shangsi section (Fig. 5). The quantitative marine biodiversity pattern indicated that no significant change in taxon richness across the WCB (Wang et al., 2014): the taxon turnover and diversification rates remained relatively stable during the Wuchiapingian but increased in the early Changhsingian, and the mean longevity of extant taxa rapidly decreased across the WCB (Fig. 4 in Wang et al., 2014). Using the temporal framework we established, onset of the prominent cooling in Meishan lags the first and second minima of $\delta^{13}C_{carb}$ by 0.73 Ma and 0.08 Ma, respectively (Fig. 3; calculation based on the accumulation rate in Supplementary Table S1). At the Shangsi section, we can only infer that the cooling phase in the *C. wangi* zone is nearly synchronous with the positive return after the broad negative shift of 6.3‰ and smaller negative shift of 3.0‰ (Fig. 5; Shen et al., 2013) due to absence of long-term $\delta^{18}O_{apatite}$ records below the WCB.

Schobben et al. (2014) reported coupled $\delta^{13}C_{carb}$ and $\delta^{18}O_{apatite}$ (IRMS) data from the Kuh-e-Ali Bashi and Zal sections in northwestern Iran, but indicated no distinct changes in both proxies from the upper Julfa Beds and lower Ali Bashi Formation, which may reflect insufficient sampling within this interval, imprecise correlation of the WCB, or another possibility that the prominent shifts in $\delta^{13}C_{carb}$ and $\delta^{18}O_{apatite}$ recorded around the WCB in Meishan and Shangsi is likely regional rather than global signals. Further long-term and high-resolution studies around the WCB in Iran, as well as other sections in South China, will be necessary to clarify whether there were any significant events occurred during the late Wuchiapingian–early Changhsingian.

6.4. Carbon cycle disruption, rapid warming, and the end-Permian mass extinction

The end-Permian CIE is widely recognized in marine and non-marine sections (Korte and Kozur, 2010; Shen et al., 2011, 2013; Payne and Clapham, 2012). Evidence from the well-constrained Meishan section indicates that the CIE started at 251.999 ± 0.039 Ma and ended at 251.572 ± 0.069 Ma, with a total duration of 427 ± 79 kyr (Burgess et al., 2014). $\delta^{13}C_{carb}$ values exhibit a gradual decrease from +3.9‰ at the beginning, followed by an abrupt decline to a minimum of −3.3‰ immediately below the mass extinction horizon before returning to +1.5‰, and subsequently end with a slight decrease to −1.7‰ (Figs. 3, 4). This pattern has been related to addition of a large amount of ^{13}C-depleted carbon into the ocean/atmosphere system, although the source remains the subject of controversy (Berner, 2002; Payne and Clapham, 2012).

The in situ SIMS technique employed on contemporaneous conodont samples across the EMPE interval from different environmental settings combined with the high-precision temporal framework, increases our understanding of the temporal and spatial pattern of seawater temperature changes prior to, during, and after the EPME (Fig. 8). The systematic offsets in $\delta^{18}O_{apatite}$ values (~1.0–1.5‰) between the carbonate platform (Daijiagou and Liangfengya) and slope (Meishan and Shangsi) correspond to the difference in CAI values (~0.5–1.0) of analyzed conodont apatite, thus indicating thermal alteration may have impacts on $\delta^{18}O_{apatite}$ values. This supports the conclusion of Wheeley et al. (2012), although an extended quantitative relationship is yet to be established. Besides this offset, data around the Permian–Triassic transition are highly comparable among studied sections. About 1.5 Ma before the onset of the end-Permian CIE (Fig. 8A), seawater temperatures fluctuate around ~18 °C. Between the onset of the CIE and the onset of the EPME (Fig. 8B), transient warming and subsequent cooling is evident among studied sections, although the timing and magnitude differ and likely suggest local controls rather than global climatic signals. Above the EPME horizon, a rapid warming is consistent in timing and magnitude (~10 °C in < 20 kyr) across shallow carbonate platform (Daijiagou and Liangfengya), upper slope (Meishan), and

lower slope (Shangsi), thus suggesting a catastrophic climatic event. Seawater temperatures remained high (>30 °C) above the PTB and continued to rise until the late Griesbachian (Sun et al., 2012; Romano et al., 2013).

Our results suggest a lag of ~25 kyr (Fig. 8B) between the rapid decline in $\delta^{13}C_{carb}$ and the rapid increase in seawater temperatures. However, the "boundary clay" at Meishan (Beds 25 and 26) was likely deposited more rapidly than the micritic limestone of Bed 27, suggesting that the lag could have been much less than 25 kyr. Global sea surface temperature does not respond quickly to climate forcing due to the thermal inertia of the ocean mixed layer and the exchange between the surface and deeper ocean (Hansen et al., 2011; Hansen and Sato, 2012). The lag of the climate response can be characterized by a climate response function, with a full response requiring at least a millennium (Hansen et al., 2011). Massive greenhouse gases released from the Siberian Traps volcanism (Svensen et al., 2009) and/or other contemporaneous volcanism (Yin et al., 1992) is likely the principal forcing that governed climate trends during the latest Permian–earliest Triassic. On millennium or longer time scales, the enhanced energy resulted from volcanic eruptions is mainly absorbed by the ocean through intake in the mixed layer and heat exchange between the surface and deeper ocean. Given a world with high continent and deep ocean during the Permian–Triassic transition (Yin and Song, 2013), full mixing in the vast Panthalassa and Tethys Oceans would take longer than usual, hence the extended delay of climate response, which makes the lag we observed plausible.

Whether rapid warming caused the catastrophic EPME depends on the pattern of mass extinction (e.g., onset, acme, and cessation). Using a confidence interval approach, the pattern of marine mass extinction was first established at the Meishan section, which revealed a single catastrophic event between Beds 25 and 28 (Jin et al., 2000). Later quantitative biostratigraphic studies using the constrained optimization approach (Shen et al., 2011; Wang et al., 2014) based a dataset of 1450 species from 18 sections across South China and the peri-Gondwanan region confirmed the conclusion that the onset and cessation of mass extinction occurred at Bed 25 and 28, respectively. Despite different views on the extinction pattern (see discussions in Wang et al., 2014), a common ground is accepted that the onset of the EPME occurred at the base of Bed 25 in Meishan. Our calculated seawater temperatures from Meishan (Figs. 4, 8B) are ~18.3 °C throughout Beds 24e and 25 (*Clarkina*), increase to 22.5 °C in Bed 26 (*Clarkina*) and then jump to 27.2 °C in Bed 27-1 (average of *Clarkina* and *Hindeodus*) before reaching a maximum of 32.4 °C in Bed 28 (*Hindeodus*). Therefore, significant warming clearly postdated the onset of the EPME, and the temperature rise cannot be considered a direct cause for the main pulse of the EPME. Nonetheless, the high rate of temperature rise (~10 °C in < 20 kyr) probably increased the pace of mass extinction, which is now constrained to have lasted for only 61 ± 48 kyr (Burgess et al., 2014).

Although our data suggests that climate warming clearly postdated the main pulse of the EPME (corresponding to Bed 25 at Meishan), we are not arguing against the involvement of the Siberian Traps volcanism in the environmental deterioration and biodiversity decline around the mass extinction horizon, since the carbon cycle disruption (Rothman et al., 2014), changes in pH (Payne et al., 2010; Hinojosa et al., 2012; Clarkson et al., 2015) and redox conditions (Cao et al., 2009) of the ocean temporally overlapped with the Siberian Traps volcanism (Burgess and Bowring, 2015). Pyroclastic and lava eruptions of the Siberian Traps began long (>200 kyr) before the initial negative shift of $\delta^{13}C_{carb}$ (Fig. 4 in Burgess and Bowring, 2015), suggesting that early explosive magmatism did not initiate dramatic feedback in the global carbon cycle. It was probably until around 251.999 ± 0.039 Ma when a tipping point was reached after sustained input and accumulation of greenhouse gases, the disruption of the carbon cycle started, followed by the abrupt negative shift of $\delta^{13}C_{carb}$ at 251.950 ± 0.042 Ma and the onset of mass extinction at 251.941 ± 0.037 Ma. Protracted degassing of CO_2 from recycled crust in the mantle plume head (Sobolev et al., 2011) provides a plausible explanation for the initial non-response and subsequent progressive decrease in $\delta^{13}C_{carb}$. By their estimation, the magnitude of the CIE would be 4.9‰ if all plume-related CO_2 migrated to the surface, and 3.5‰ with the migration of only half of the volume (Sobolev et al., 2011). Judging from the overall trend and magnitude of the CIE (Korte and Kozur, 2010; Shen et al., 2013), it is likely only around half of the plume-related CO_2 was released prior to the onset of the EPME. The rapid decline of $\delta^{13}C_{carb}$ across the mass extinction horizon and continuing negative shift in the earliest Triassic are probably the consequences of subsequent massive release through contact metamorphism of carbon-rich and sulfur-rich sediments (Erwin, 2006; Svensen et al., 2009), superimposed on the remnant plume-related degassing.

In the absence of robust evidence to identify main pulse(s) of the Siberian Traps volcanism, our seawater temperature record may be interpreted as an indirect monitor for the volcanic processes. A new age model for the extrusive and intrusive magmatism of the Siberian Traps (Burgess and Bowring, 2015) suggested that the majority of extrusive magmatism occurred between 252.20 ± 0.12 Ma and 251.901 ± 0.061 Ma, and the intrusive magmatism started at 251.907 ± 0.067 Ma and continued for at least 500 kyr after the cessation of mass extinction. If we accept that the substantial temperature rise occurred in Beds 27–28 at Meishan (Fig. 8B) and consider the potentially biased sample coverage for the older sills (Burgess and Bowring, 2015), a restricted interval of the overlap (~251.918–251.880 Ma) between the lave eruption and intrusive magmatism is likely responsible for the rapid climate warming.

7. Conclusions

In situ oxygen isotope analyses on conodont apatite from four sections in South China (Meishan, Shangsi, Daijiagou, and Liangfengya) provides a high-resolution relative seawater temperature record of the Late Permian–Early Triassic. Constrained by the latest high-precision geochronology and high-resolution conodont biostratigraphy, we can place the temperatures in both temporal and spatial perspectives. Coupled with $\delta^{13}C_{carb}$ data and biodiversity pattern, our results shed light on the causal links between the environmental changes and biological crisis, especially across the catastrophic EPME interval. Key findings in this study are:

(1) A prominent cooling occurred in the earliest Changhsingian, with the main phase (a drop of ~8 °C in ~0.2 Ma) confined to the lower part of the *C. wangi* zone and synchronous with the positive limb of the CIE around the WCB at Meishan and Shangsi. Full contexts and underlying dynamics of the "WCB events" await further confirmation from other sections.

(2) After the cooling event, seawater temperatures fluctuated during most the Changhsingian. Transient warming and subsequent cooling is recorded between the onset of negative shift in $\delta^{13}C_{carb}$ and the onset of the EMPE, which probably represents the last pulse of the long-term fluctuations rather than any significant climatic events. Evidence such as gradual decline in $\delta^{13}C_{carb}$ and the absence of substantial changes in the temperature record suggests that the Siberian Traps magmatism and/or other contemporaneous volcanism had not reached their full potential at the onset of mass extinction.

(3) Above the extinction horizon, a dramatic warming (~10 °C in < 20 kyr) is consistent in timing and magnitude across the upper slope (Meishan), lower slope (Shangsi), and carbonate platform (Daijiagou and Liangfengya), companied with ocean acidification and continued decrease in $\delta^{13}C_{carb}$, thus indicating a catastrophic event that is likely related to massive degassing during a restricted interval (~251.918–251.880 Ma) of the Siberian Traps volcanism.

(4) The lags between the abrupt decline in $\delta^{13}C_{carb}$, the onset of the EMPE, and the rapid temperature increase suggest that climate

warming was most likely not a direct cause for the main pulse of the EPME (corresponding to Bed 25 at Meishan), but rather a later participant or a catalyst that increased the pace of the biodiversity decline.

(5) Comparison based on a suite of 63 conodont samples from the Meishan section that have been measured by both SIMS and IRMS methods suggests that the SIMS $\delta^{18}O_{apatite}$ values are generally higher that the IRMS ones, with an average offset of +0.5‰.

Acknowledgments

We thank G.Q. Tang, Y. Liu, X.X. Ling, and H.X. Ma for assistance with the SIMS analyses. We are also grateful to Zivile Zigaite and Charles Henderson for their constructive reviews and Jisuo Jin for his editorial handling. This research was supported by the National Natural Science Foundation of China (41290260, 41203008), National Basic Research Program of China (2011CB808900), State Key Laboratory of Isotope Geochemistry (SKLIG-QD-12-02), and State Key Laboratory of Palaeobiology and Stratigraphy (123111, 20131101). S.A. Bowring's participation was supported by the National Science Foundation (EAR-0807475). This is contribution No. IS-2162 from GIGCAS.

Appendix A. Supplementary data

Supplementary data associated with this article can be found in the online version, at http://dx.doi.org/10.1016/j.palaeo.2015.11.025. These data include the Google map of the most important areas described in this article.

Appendix A. Supplementary data

Supplementary data to this article can be found online at http://dx.doi.org/10.1016/j.palaeo.2015.11.025.

References

Adkins, J.F., McIntyre, K., Schrag, D.P., 2002. The salinity, temperature, and $\delta^{18}O$ of the glacial deep ocean. Science 298, 1769–1773.

Aubert, M., Williams, I.S., Boljkovac, K., Moffat, I., Moncel, M.H., Dufour, E., Grun, R., 2012. In situ oxygen isotope micro-analysis of faunal material and human teeth using a SHRIMP II: a new tool for palaeo-ecology and archaeology. J. Archaeol. Sci. 39, 3184–3194.

Beauchamp, B., Baud, A., 2002. Growth and demise of Permian biogenic chert along northwest Pangea: evidence for end-Permian collapse of thermohaline circulation. Palaeogeogr. Palaeoclimatol. Palaeoecol. 184, 37–63.

Berner, R.A., 2002. Examination of hypotheses for the Permo-Triassic boundary extinction by carbon cycle modeling. Proc. Natl. Acad. Sci. U. S. A. 99, 4172–4177.

Black, B.A., Elkins-Tanton, L.T., Rowe, M.C., Peate, I.U., 2012. Magnitude and consequences of volatile release from the Siberian Traps. Earth Planet. Sci. Lett. 317, 363–373.

Blumenthal, S.A., Cerling, T.E., Chritz, K.L., Bromage, T.G., Kozdon, R., Valley, J.W., 2014. Stable isotope time-series in mammalian teeth: In situ $\delta^{18}O$ from the innermost enamel layer. Geochim. Cosmochim. Acta 124, 223–236.

Bond, D.P.G., Wignall, P.B., 2014. Large igneous provinces and mass extinctions: an update. In: Keller, G., Kerr, A.C. (Eds.), Volcanism, Impacts, and Mass Extinctions: Causes and Effects: Geological Society of America Special Paper 505. The Geological Society of America, Boulder, pp. 29–55.

Burgess, S.D., Bowring, S., 2015. High-precision geochronology confirms voluminous magmatism before, during, and after Earth's most severe extinction. Sci. Adv. 1, e1500470.

Burgess, S.D., Bowring, S.A., Shen, S.Z., 2014. High-precision timeline for Earth's most severe extinction. Proc. Natl. Acad. Sci. U. S. A. 111, 3316–3321.

Campbell, I.H., Czamanske, G.K., Fedorenko, V.A., Hill, R.I., Stepanov, V., 1992. Synchronism of the Siberian Traps and the Permian–Triassic Boundary. Science 258, 1760–1763.

Cao, C.Q., Zheng, Q.F., 2007. High-resolution lithostratigraphy of the Changhsingian stage in Meishan section D, Zhejiang. J. Stratigr. 31, 14–22.

Cao, C.Q., Love, G.D., Hays, L.E., Wang, W., Shen, S.Z., Summons, R.E., 2009. Biogeochemical evidence for euxinic oceans and ecological disturbance presaging the end-Permian mass extinction event. Earth Planet. Sci. Lett. 281, 188–201.

Chang, S.J., Blake, R.E., 2015. Precise calibration of equilibrium oxygen isotope fractionations between dissolved phosphate and water from 3 to 37 °C. Geochim. Cosmochim. Acta 150, 314–329.

Chen, B., Joachimski, M.M., Sun, Y.D., Shen, S.Z., Lai, X.L., 2011. Carbon and conodont apatite oxygen isotope records of Guadalupian–Lopingian boundary sections: climatic or sea-level signal? Palaeogeogr. Palaeoclimatol. Palaeoecol. 311, 145–153.

Chen, B., Joachimski, M.M., Shen, S.Z., Lambert, L.L., Lai, X.L., Wang, X.D., Chen, J., Yuan, D.X., 2013. Permian ice volume and palaeoclimate history: oxygen isotope proxies revisited. Gondwana Res. 24, 77–89.

Chumakov, N.M., Zharkov, M.A., 2003. Climate during the Permian–Triassic biosphere reorganizations. Article 2. Climate of the Late Permian and Early Triassic: general inferences. Stratigr. Geol. Correl. 11, 361–375.

Clarkson, M.O., Kasemann, S.A., Wood, R.A., Lenton, T.M., Daines, S.J., Richoz, S., Ohnemueller, F., Meixner, A., Poulton, S.W., Tipper, E.T., 2015. Ocean acidification and the Permo-Triassic mass extinction. Science 348, 229–232.

Conroy, J.L., Cobb, K.M., Lynch-Stieglitz, J., Polissar, P.J., 2014. Constraints on the salinity–oxygen isotope relationship in the central tropical Pacific Ocean. Mar. Chem. 161, 26–33.

Erwin, D.H., 2006. Extinction: How Life on Earth Nearly Ended 250 Million Years Ago. Princeton University Press, Princeton, N.J.

Fielding, C.R., Frank, T.D., Birgenheier, L.P., Rygel, M.C., Jones, A.T., Roberts, J., 2008. Stratigraphic imprint of the Late Palaeozoic Ice Age in eastern Australia: a record of alternating glacial and nonglacial climate regime. J. Geol. Soc. Lond. 165, 129–140.

Frank, T.D., Shultis, A.I., Fielding, C.R., 2015. Acme and demise of the late Palaeozoic ice age: a view from the southeastern margin of Gondwana. Palaeogeogr. Palaeoclimatol. Palaeoecol. 418, 176–192.

Hansen, J., Sato, M., 2012. Paleoclimate implications for human-made climate change. In: Berger, A., Mesinger, F., Sijacki, D. (Eds.), Climate Change. Springer-Verlag Wien, Vienna, pp. 21–47.

Hansen, J., Sato, M., Kharecha, P., von Schuckmann, K., 2011. Earth's energy imbalance and implications. Atmos. Chem. Phys. 11, 13421–13449.

Henderson, C.M., 2006. Beware of your FO and be aware of the FAD. Permophiles 47, 8–9.

Hinojosa, J.L., Brown, S.T., Chen, J., DePaolo, D.J., Paytan, A., Shen, S.Z., Payne, J.L., 2012. Evidence for end-Permian ocean acidification from calcium isotopes in biogenic apatite. Geology 40, 743–746.

Holser, W.T., Schönlaub, H.P., Attrep, M., Boeckelmann, K., Klein, P., Magaritz, M., Orth, C.J., Fenninger, A., Jenny, C., Kralik, M., Mauritsch, H., Pak, E., Schramm, J.M., Stattegger, K., Schmoller, R., 1989. A unique geochemical record at the Permian/Triassic boundary. Nature 337, 39–44.

Jaffrés, J.B.D., Shields, G.A., Wallmann, K., 2007. The oxygen isotope evolution of seawater: a critical review of a long-standing controversy and an improved geological water cycle model for the past 3.4 billion years. Earth-Sci. Rev. 83, 83–122.

Jiang, H.S., Lai, X.L., Yan, C.B., Aldridge, R.J., Wignall, P., Sun, Y.D., 2011. Revised conodont zonation and conodont evolution across the Permian–Triassic boundary at the Shangsi section, Guangyuan, Sichuan, South China. Glob. Planet. Chang. 77, 103–115.

Jin, Y.G., Wang, Y., Wang, W., Shang, Q.H., Cao, C.Q., Erwin, D.H., 2000. Pattern of marine mass extinction near the Permian–Triassic boundary in South China. Science 289, 432–436.

Jin, Y.G., Wang, Y., Henderson, C., Wardlaw, B.R., Shen, S.Z., Cao, C.Q., 2006. The Global Boundary Stratotype Section and Point (GSSP) for the base of Changhsingian Stage (Upper Permian). Episodes 29, 175–182.

Joachimski, M.M., Breisig, S., Buggisch, W., Talent, J.A., Mawson, R., Gereke, M., Morrow, J.R., Day, J., Weddige, K., 2009. Devonian climate and reef evolution: insights from oxygen isotopes in apatite. Earth Planet. Sci. Lett. 284, 599–609.

Joachimski, M.M., Lai, X.L., Shen, S.Z., Jiang, H.S., Luo, G.M., Chen, B., Chen, J., Sun, Y.D., 2012. Climate warming in the latest Permian and the Permian–Triassic mass extinction. Geology 40, 195–198.

Kamo, S.L., Czamanske, G.K., Amelin, Y., Fedorenko, V.A., Davis, D.W., Trofimov, V.R., 2003. Rapid eruption of Siberian flood-volcanic rocks and evidence for coincidence with the Permian–Triassic boundary and mass extinction at 251 Ma. Earth Planet. Sci. Lett. 214, 75–91.

Knoll, A.H., Bambach, R.K., Payne, J.L., Pruss, S., Fischer, W.W., 2007. Paleophysiology and end-Permian mass extinction. Earth Planet. Sci. Lett. 256, 295–313.

Kolodny, Y., Luz, B., Navon, O., 1983. Oxygen isotope variations in phosphate of biogenic apatites, I. Fish bone apatite — rechecking the rules of the game. Earth Planet. Sci. Lett. 64, 298–404.

Korte, C., Kozur, H.W., 2010. Carbon-isotope stratigraphy across the Permian–Triassic boundary: a review. J. Asian Earth Sci. 39, 215–235.

Kozdon, R., Ushikubo, T., Kita, N.T., Spicuzza, M., Valley, J.W., 2009. Intratest oxygen isotope variability in the planktonic foraminifer *N. pachyderma*: real vs. apparent vital effects by ion microprobe. Chem. Geol. 258, 327–337.

Kozdon, R., Kelly, D.C., Kita, N.T., Fournelle, J.H., Valley, J.W., 2011. Planktonic foraminiferal oxygen isotope analysis by ion microprobe technique suggests warm tropical sea surface temperatures during the Early Paleogene. Paleoceanography 26.

Kummel, B., Teichert, C., 1970. Stratigraphy and paleontology of the Permian–Triassic boundary beds, salt range and trans-Indus ranges, West Pakistan. In: Kummel, B., Teichert, C. (Eds.), Stratigraphic Boundary Problems–Permian and Triassic of West Pakistan. The University Press of Kansas, Lawrence, pp. 1–110.

Lécuyer, C., Amiot, R., Touzeau, A., Trotter, J., 2013. Calibration of the phosphate $d^{18}O$ thermometer with carbonate–water oxygen isotope fractionation equations. Chem. Geol. 347, 217–226.

Lhomme, N., Clarke, G.K.C., Ritz, C., 2005. Global budget of water isotopes inferred from polar ice sheets. Geophys. Res. Lett. 32, L20502.

Luz, B., Kolodny, Y., 1985. Oxygen isotope variations in phosphate of biogenic apatites, IV. Mammal teeth and bones. Earth Planet. Sci. Lett. 75, 29–36.

Luz, B., Kolodny, Y., Kovach, J., 1984. Oxygen isotope variations in phosphate of biogenic apatites, III. Conodonts. Earth Planet. Sci. Lett. 69, 255–262.

Mei, S.L., Henderson, C.M., 2001. Evolution of Permian conodont provincialism and its significance in global correlation and paleoclimate implication. Palaeogeogr. Palaeoclimatol. Palaeoecol. 170, 237–260.
Metcalfe, I., Crowley, J.L., Nicoll, R.S., Schmitz, M., 2015. High-precision U–Pb CA–TIMS calibration of Middle Permian to Lower Triassic sequences, mass extinction and extreme climate-change in eastern Australian Gondwana. Gondwana Res. 28, 61–81.
Nicoll, R.S., Metcalfe, I., Wang, C.Y., 2002. New species of the conodont genus *Hindeodus* and the conodont biostratigraphy of the Permian–Triassic boundary interval. J. Asian Earth Sci. 20, 609–631.
O'Neil, J.R., Roe, L.J., Reinhard, E., Blake, R.E., 1994. A rapid and precise method of oxygen isotope analysis of biogenic phosphate. Isr. J. Earth Sci. 43, 203–212.
Payne, J.L., Clapham, M.E., 2012. End-Permian mass extinction in the oceans: an ancient analog for the twenty-first century? Annu. Rev. Earth Planet. Sci. 40, 89–111.
Payne, J.L., Turchyn, A.V., Paytan, A., DePaolo, D.J., Lehrmann, D.J., Yu, M.Y., Wei, J.Y., 2010. Calcium isotope constraints on the end-Permian mass extinction. Proc. Natl. Acad. Sci. U. S. A. 107, 8543–8548.
Pietzner, H., Vahl, J., Werner, H., Ziegler, W., 1968. Zur chemischen Zusammensetzung und Mikromorphologie der Conodonten. Palaeontographica 128, 115–152.
Pucéat, E., Joachimski, M.M., Bouilloux, A., Monna, F., Bonin, A., Motreuil, S., Moriniere, P., Henard, S., Mourin, J., Dera, G., Quesne, D., 2010. Revised phosphate–water fractionation equation reassessing paleotemperatures derived from biogenic apatite. Earth Planet. Sci. Lett. 298, 135–142.
Raup, D.M., Sepkoski, J.J., 1982. Mass extinctions in the marine fossil record. Science 215, 1501–1503.
Renne, P.R., Zhang, Z.C., Richards, M.A., Black, M.T., Basu, A.R., 1995. Synchrony and causal relations between Permian–Triassic boundary crises and Siberian flood volcanism. Science 269, 1413–1416.
Rey, K., Amiot, R., Fourel, F., Rigaudier, T., Abdala, F., Day, M.O., Fernandez, V., Fluteau, F., France-Lanord, C., Rubidge, B.S., Smith, R.M., Viglietti, P.A., Zipfel, B., Lécuyer, C., 2015. Global climate perturbations during the Permo-Triassic mass extinctions recorded by continental tetrapods from South Africa. Gondwana Res. http://dx.doi.org/10.1016/j.gr.2015.09.008 (in press).
Rigo, M., Trotter, J.A., Preto, N., Williams, I.S., 2012. Oxygen isotopic evidence for Late Triassic monsoonal upwelling in the northwestern Tethys. Geology 40, 515–518.
Romano, C., Goudemand, N., Vennemann, T.W., Ware, D., Schneebeli-Hermann, E., Hochuli, P.A., Bruhwiler, T., Brinkmann, W., Bucher, H., 2013. Climatic and biotic upheavals following the end-Permian mass extinction. Nat. Geosci. 6, 57–60.
Rothman, D.H., Fournier, G.P., French, K.L., Alm, E.J., Boyle, E.A., Cao, C.Q., Summons, R.E., 2014. Methanogenic burst in the end-Permian carbon cycle. Proc. Natl. Acad. Sci. U. S. A. 111, 5462–6467.
Schobben, M., Joachimski, M.M., Korn, D., Leda, L., Korte, C., 2014. Palaeotethys seawater temperature rise and an intensified hydrological cycle following the end-Permian mass extinction. Gondwana Res. 26, 675–683.
Shemesh, A., Kolodny, Y., Luz, B., 1983. Oxygen isotope variations in phosphate of biogenic apatites, II. Phosphorite rocks. Earth Planet. Sci. Lett. 64, 405–416.
Shen, S.Z., He, X.L., 1991. Changhsingian brachiopods assemblage sequence in Zhongliang Hill, Chongqing. J. Stratigr. 15, 189–196.
Shen, S.Z., Mei, S.L., 2010. Lopingian (Late Permian) high-resolution conodont biostratigraphy in Iran with comparison to South China zonation. Geol. J. 45, 135–161.
Shen, S.Z., Shi, G.R., 1995. Biostratigraphy and correlation of several Permian–Triassic boundary sections in southwestern China. J. SE Asian Earth Sci. 12, 19–30.
Shen, S.Z., Shi, G.R., 2002. Paleobiogeographical extinction patterns of Permian brachiopods in the Asian-western Pacific region. Paleobiology 28, 449–463.
Shen, S.Z., Cao, C.Q., Henderson, C.M., Wang, X.D., Shi, G.R., Wang, Y., Wang, W., 2006. End-Permian mass extinction pattern in the northern peri-Gondwanan region. Palaeoworld 15, 3–30.
Shen, S.Z., Henderson, C.M., Bowring, S.A., Cao, C.Q., Wang, Y., Wang, W., Zhang, H., Zhang, Y.C., Mu, L., 2010. High-resolution Lopingian (Late Permian) timescale of South China. Geol. J. 45, 122–134.
Shen, S.Z., Crowley, J.L., Wang, Y., Bowring, S.A., Erwin, D.H., Sadler, P.M., Cao, C.Q., Rothman, D.H., Henderson, C.M., Ramezani, J., Zhang, H., Shen, Y.N., Wang, X.D., Wang, W., Mu, L., Li, W.Z., Tang, Y.G., Liu, X.L., Liu, L.J., Zeng, Y., Jiang, Y.F., Jin, Y.G., 2011. Calibrating the end-Permian mass extinction. Science 334, 1367–1372.
Shen, S.Z., Cao, C.Q., Zhang, H., Bowring, S.A., Henderson, C.M., Payne, J.L., Davydov, V.I., Chen, B., Yuan, D.X., Zhang, Y.C., Wang, W., Zheng, Q.F., 2013. High-resolution $d^{13}C_{carb}$ chemostratigraphy from latest Guadalupian through earliest Triassic in South China and Iran. Earth Planet. Sci. Lett. 375, 156–165.
Sobolev, S.V., Sobolev, A.V., Kuzmin, D.V., Krivolutskaya, N.A., Petrunin, A.G., Arndt, N.T., Radko, V.A., Vasiliev, Y.R., 2011. Linking mantle plumes, large igneous provinces and environmental catastrophes. Nature 477, 312–316.
Song, H.J., Wignall, P.B., Tong, J.N., Yin, H.F., 2013. Two pulses of extinction during the Permian–Triassic crisis. Nat. Geosci. 6, 52–56.
Stampfli, G.M., Borel, G.D., 2004. The TRANSMED transects in space and time: constraints on the paleotectonic evolution of the Mediterranean domain. In: Cavazza, W., Rouce, F., Spakman, W., Stampfli, G.M., Ziegler, P. (Eds.), The TRANSMED Atlas: The Mediterranean Region from Crust to Mantle. Springer, Berlin Heidelberg, pp. 1–141.
Sun, Y.D., Joachimski, M.M., Wignall, P.B., Yan, C.B., Chen, Y.L., Jiang, H.S., Wang, L.N., Lai, X.L., 2012. Lethally hot temperatures during the Early Triassic greenhouse. Science 338, 366–370.
Svensen, H., Planke, S., Polozov, A.G., Schmidbauer, N., Corfu, F., Podladchikov, Y.Y., Jamtveit, B., 2009. Siberian gas venting and the end-Permian environmental crisis. Earth Planet. Sci. Lett. 277, 490–500.
Trotter, J.A., Williams, I.S., Barnes, C.R., Lécuyer, C., Nicoll, R.S., 2008. Did cooling oceans trigger Ordovician biodiversification? Evidence from conodont thermometry. Science 321, 550–554.
Trotter, J.A., Williams, I.S., Nicora, A., Mazza, M., Rigo, M., 2015. Long-term cycles of Triassic climate change: a new $\delta^{18}O$ record from conodont apatite. Earth Planet. Sci. Lett. 415, 165–174.
Wang, Y., Shen, S.Z., Cao, C.Q., Wang, W., Henderson, C.M., Jin, Y.G., 2006. The Wuchiapingian–Changhsingian boundary (Upper Permian) at Meishan of Changxing County, South China. J. Asian Earth Sci. 26, 575–583.
Wang, Y., Sadler, P.M., Shen, S.Z., Erwin, D.H., Zhang, Y.C., Wang, X.D., Wang, W., Crowley, J.L., Henderson, C.M., 2014. Quantifying the process and abruptness of the end-Permian mass extinction. Paleobiology 40, 113–129.
Wardlaw, B.R., Mei, S.L., 1999. Refined conodont biostratigraphy of the Permian and lowest Triassic of the Salt and Khizor Ranges, Pakistan. In: Ying, H.F., Tong, J.N. (Eds.), Proceedings of the International conference on Pangea and the Paleozoic–Mesozoic transition. China University of Geosciences Press, Wuhan, pp. 154–156.
Wenzel, B., Lécuyer, C., Joachimski, M.M., 2000. Comparing oxygen isotope records of Silurian calcite and phosphate — $\delta^{18}O$ compositions of brachiopods and conodonts. Geochim. Cosmochim. Acta 64, 1859–1872.
Wheeley, J.R., Smith, M.P., Boomer, I., 2012. Oxygen isotope variability in conodonts: implications for reconstructing Palaeozoic palaeoclimates and palaeoceanography. J. Geol. Soc. Lond. 169, 239–250.
Wignall, P.B., 2001. Large igneous provinces and mass extinctions. Earth-Sci. Rev. 53, 1–33.
Wignall, P.B., Hallam, A., 1996. Facies change and the end-Permian mass extinction in S.E. Sichuan, China. Palaios 11, 587–596.
Yin, H.F., Song, H.J., 2013. Mass extinction and Pangea integration during the Paleozoic–Mesozoic transition. Sci. China Ser. D 56, 1791–1803.
Yin, H.F., Huang, S., Zhang, K.X., Hansen, H.J., Yang, F.Q., Ding, M.H., Bie, X.M., 1992. The effects of volcanism on the Permo-Triassic mass extinction in South China. In: Sweet, W.C., Yang, Z.Y., Dickins, J.M., Ying, H.F. (Eds.), Permo-Triassic Events in the Eastern Tethys. Cambridge University Press, Cambridge, pp. 146–157.
Yin, H.F., Zhang, K.X., Tong, J.N., Yang, Z.Y., Wu, S.B., 2001. The Global Stratotype Section and Point (GSSP) of the Permian–Triassic Boundary. Episodes 24, 102–114.
Yin, H.F., Jiang, H.S., Xia, W.C., Feng, Q.L., Zhang, N., Shen, J., 2014. The end-Permian regression in South China and its implication on mass extinction. Earth-Sci. Rev. 137, 19–33.
Yuan, D.X., Shen, S.Z., 2011. Conodont succession across the Permian–Triassic boundary at the Liangfengya section, Chongqing, South China. Acta Palaeontol. Sin. 50, 420–438.
Yuan, D.X., Shen, S.Z., Henderson, C.M., Chen, J., Zhang, H., Feng, H.Z., 2014. Revised conodont-based integrated high-resolution timescale for the Changhsingian Stage and end-Permian extinction interval at the Meishan sections, South China. Lithos 204, 220–245.
Yuan, D.X., Chen, J., Zhang, Y.C., Zheng, Q.F., Shen, S.Z., 2015. Changhsingian conodont succession and the end-Permian mass extinction event at the Daijiagou section in Chongqing, Southwest China. J. Asian Earth Sci. 105, 234–251.
Zigaite, Z., Whitehouse, M., 2014. Stable oxygen isotopes of dental biomineral: differentiation at the intra- and inter-tissue level of modern shark teeth. GFF 136, 337–340.